Published by :
https://www.ijert.org/
An International Peer-Reviewed Journal

International Journal of Engineering Research & Technology (IJERT)
ISSN: 2278-0181
Vol. 15 Issue 10 , October - 2026

Compact Beveled Y-Shaped Monopole Antenna with Two Matched UWB Sub-Bands for Off-Body Wearable Communication: A Simulation Study

Selvakumari J
ME Communication System
Dept. of Electronics and Communication Engineering.
PET Engineering College, Vallioor, Tirunelveli

Dr. R. S.Ganesh
Professor
Dept. of Electronics and Communication Engineering.
PET Engineering College, Vallioor, Tirunelveli

Abstract:
Wearable off-body links need antennas that stay matched next to the body while keeping absorbed power low. This paper presents the simulated design and characterisation of a compact, planar, beveled Y-shaped monopole on Rogers RO4003 (60 × 60 × 1.6 mm) with slotted front and rear metallisation and a partial ground plane, intended as the radiating element of a future AMC-backed wearable antenna. ANSYS HFSS 2025 simulation gives resonances at 3.8 GHz (S11 = −13.72 dB) and 7.12 GHz (−25.80 dB), with S11 ≤ −10 dB over 3.43–4.51 GHz and 5.79–8.39 GHz. These two bands cover about 49 % of the 3.1–10.6 GHz UWB allocation, so the antenna does not cover the entire UWB range. The E-plane pattern is omnidirectional with about 15 dB co-/cross-polar isolation, and the peak gain is 3.98 dB. For one simulated placement near the body the SAR is 1.2866 W/kg against a 1 g, 1.6 W/kg limit; the tissue model, spacing and input power were not recorded, so no compliance is claimed beyond that case. Bandwidth and pattern are reported as retained on 30 mm and 40 mm cylinders, but numerical resonance shifts are not available. The paper does not claim higher gain or lower SAR than EBG-backed designs. Its contribution is a documented planar baseline, a coverage and power accounting of the matched bands, and an explicit list of the evidence still needed before the design can be judged. All results are simulated; no prototype has been measured.

Keywords: Wearable antenna, ultra-wideband, WBAN, off-body communication, specific absorption rate, bending, artificial magnetic conductor, ANSYS HFSS.

I. INTRODUCTION

Wearable wireless communication systems have gained increasing attention in healthcare monitoring, personal safety, and wireless body-area networks (WBANs). These systems enable body-worn devices to transmit physiological and other sensor information to external receivers without requiring wired connections. IEEE 802.15.6 defines physical-layer technologies for WBAN communication, including narrowband, ultra-wideband (UWB), and human-body communication approaches [1]. Among these technologies, UWB is attractive for short-range wireless applications because of its wide operating bandwidth, high data-rate potential, and suitability for precise time-domain measurements. The Federal Communications Commission (FCC) specifies an unlicensed UWB operating range of 3.1–10.6 GHz under defined emission limits [2]. However, designing an antenna for wearable UWB communication involves more than achieving impedance matching across a frequency range. The proximity of the human body can influence antenna impedance, radiation characteristics, and electromagnetic energy distribution. In addition, the amount of power absorbed by biological tissue must be considered when evaluating an antenna intended for prolonged body-worn operation [3], [4]. Therefore, impedance bandwidth, radiation behaviour, gain, bending response, and specific absorption rate (SAR) are important parameters in wearable antenna assessment. Printed monopole antennas are suitable candidates for compact wireless devices because of their planar construction, relatively simple fabrication, and adaptability to different radiator and ground-plane geometries. Their electromagnetic characteristics can be modified through changes in patch dimensions, feed configuration, slots, and ground-plane structure. Nevertheless, a compact monopole that provides acceptable impedance matching does not necessarily produce favourable radiation away from the body or sufficiently low tissue absorption. These aspects require separate evaluation under clearly defined simulation or measurement conditions. Electromagnetic band-gap (EBG) and artificial magnetic conductor (AMC) structures have been investigated as possible approaches to controlling backward radiation and reducing electromagnetic coupling between wearable antennas and the human body [5]–[7]. Their performance depends on the unit-cell configuration, substrate properties, operating frequency, and separation between the radiator and the backing structure. Consequently, improvements reported

(This work is licensed under a Creative Commons Attribution 4.0 International License.)

International Journal of Engineering Research & Technology (IJERT)
ISSN: 2278-0181
Vol. 15 Issue 10 , October - 2026

for an EBG- or AMC-backed antenna cannot automatically be attributed to an unbacked radiator or transferred to a different antenna geometry without further evaluation. In this work, a compact, planar, beveled Y-shaped monopole antenna is modelled on a Rogers RO4003 substrate with overall dimensions of 60 × 60 × 1.6 mm³. The proposed geometry incorporates slotted front- and rear-side metallisation, an inset feed, and a partial ground plane. ANSYS HFSS 2025 is used to investigate its simulated impedance response, resonant frequencies, radiation characteristics, surface-current distribution, and behaviour under selected cylindrical bending configurations. The design exhibits two matched frequency bands, extending from 3.43 to 4.51 GHz and from 5.79 to 8.39 GHz, with resonances at 3.8 and 7.12 GHz, respectively. These results represent partial coverage of the 3.1–10.6 GHz UWB allocation rather than continuous matching across the entire range. The study also examines the reported gain, radiation pattern, and body-proximity SAR under the available simulation configuration. The simulated SAR value is 1.2866 W/kg for the evaluated placement, compared with the stated 1 g limit of 1.6 W/kg. However, the available documentation does not provide all the tissue-model, antenna-to-body spacing, and input-power details required to establish general exposure compliance. Similarly, the bending response is considered for 30 mm and 40 mm cylindrical configurations, although numerical resonance shifts are not available. The antenna is evaluated as a planar baseline radiator for possible future AMC integration; an AMC-backed configuration and experimental prototype are not part of the present study.

The main contributions of this work are decribed below as follows :

1. A compact beveled Y-shaped monopole antenna with slotted metallisation and a partial ground plane is modelled using ANSYS HFSS 2025.
2. The two simulated resonant frequencies and their corresponding −10 dB impedance-matched frequency bands are characterised, with the extent of UWB coverage explicitly identified.
3. The radiation characteristics, gain, surface-current distribution, and response under selected cylindrical bending configurations are examined.
4. The available body-proximity SAR result is reported with its evaluation limitations, avoiding unsupported claims of general exposure compliance.
5. The resulting simulation data establish a baseline for subsequent AMC integration, comparative electromagnetic evaluation, and experimental validation.

The remainder of this paper is organised as follows. Section II discusses the background and theoretical concepts relevant to wearable communication and antenna design. Section III reviews related work on compact UWB, button-type, textile, and EBG- or AMC-backed wearable antennas. Section IV describes the antenna geometry and simulation methodology. Section V presents and discusses the simulated results. Section VI discusses the limitations and future development of the antenna, while Section VII concludes the paper.

II. BACKGROUND AND THEORY

A. WBAN Communication Scenarios

Wireless Body Area Networks (WBANs) enable communication between electronic devices operating on, inside, or around the human body. Based on the location of the communicating devices, WBAN communication is generally classified into three categories: in-body, on-body, and off-body communication. In-body communication involves implanted or ingestible devices that transmit information through biological tissue. On-body communication connects wearable devices positioned on the body surface, whereas off-body communication establishes a wireless link between a body-mounted device and an external receiver [3]. The present study focuses on off-body communication, in which the antenna is expected to transfer electromagnetic energy towards an external access point while operating in proximity to the human body. Antenna performance in this configuration depends on impedance matching, radiation characteristics, body-induced detuning, and electromagnetic energy absorbed by surrounding tissue. Therefore, the evaluation of wearable antennas requires consideration of both free-space radiation performance and their behaviour under body-proximity conditions. IEEE 802.15.6 defines physical-layer technologies for WBAN applications, including narrowband, ultra-wideband, and human-body communication [1]. UWB-based wearable systems provide one possible approach for short-range wireless connectivity where bandwidth and time-resolution characteristics are important.

B. Application Scenarios

Wearable antennas are relevant to several applications that require reliable communication between body-mounted devices and external receivers. In remote healthcare monitoring, wearable sensors transmit physiological information to nearby monitoring equipment. Their antennas should maintain an acceptable communication link during changes in body posture and movement. In defence and public-safety applications, wearable communication devices support the exchange of personnel information with external monitoring stations. These systems require compact antenna structures with consistent radiation characteristics under different operating conditions. Similarly, smartwatches and fitness-monitoring devices require antennas that can operate within restricted physical dimensions while maintaining suitable wireless connectivity. These applications establish three important design considerations: compact physical

(This work is licensed under a Creative Commons Attribution 4.0 International License.)

International Journal of Engineering Research & Technology (IJERT)
ISSN: 2278-0181
Vol. 15 Issue 10 , October - 2026

dimensions, stable electromagnetic performance, and controlled interaction with nearby biological tissue. The antenna investigated in this work is therefore considered a candidate radiating element for future off-body wearable communication systems.

C. Ultra-Wideband Technology

Ultra-wideband technology is characterised by its wide operating bandwidth and suitability for short-range wireless communication. The 3.1–10.6 GHz frequency allocation is commonly associated with UWB applications under the applicable regulatory emission restrictions [2]. The large available bandwidth supports high data-rate communication and provides improved temporal resolution for applications involving ranging and positioning. UWB signals can also provide resistance to narrowband interference under appropriate transmission and reception conditions. These characteristics make the technology relevant to compact wireless devices and wearable communication systems. However, the wide operating bandwidth introduces additional requirements for antenna design. The antenna should maintain suitable impedance matching and radiation characteristics throughout its intended operating bands. For pulse-based communication, frequency-dependent variations in phase and group delay must also be considered because they can affect the transmitted waveform. In this study, the antenna is evaluated over a simulated frequency sweep of 2–12 GHz. Its matched frequency regions are identified using the −10 dB reflection-coefficient criterion and compared with the 3.1–10.6 GHz UWB allocation.

D. Microstrip-Fed Monopole Antennas

Printed monopole antennas are commonly investigated for compact wireless applications because their planar construction supports relatively simple fabrication and integration. A typical structure consists of a radiating element, dielectric substrate, ground plane, and feeding arrangement. The electrical characteristics depend on the dimensions of the radiator, substrate properties, feed configuration, and ground-plane geometry [9]. A microstrip feeding arrangement provides a planar connection between the antenna and its excitation port. Inset feeding allows the input impedance to be adjusted by changing the feed position within the radiating element. This approach is useful when matching the antenna to a 50 Ω source without introducing an additional impedance-transforming section. The main alternatives include coaxial-probe, aperture-coupled, and proximity-coupled feeding techniques. Their structural requirements differ in terms of substrate penetration, additional layers, and fabrication complexity

Feed	Structure	Wearable suitability
Inset microstrip line	Planar, single layer	High; relatively simple fabrication and impedance adjustment
Coaxial probe	Probe through substrate	Lower; requires additional mechanical support
Aperture coupled	Multilayer configuration	Moderate; requires layer alignment
Proximity coupled	Multilayer configuration	Moderate; comparatively complex fabrication

Table I. Comparison of feeding techniques for microstrip antennas

For the present antenna, an inset microstrip feeding arrangement is adopted to maintain a planar structure and provide an adjustable input impedance. The final feed dimensions are established through electromagnetic simulation.

E. Artificial Magnetic Conductor Backing

An Artificial Magnetic Conductor (AMC) is a periodic electromagnetic structure designed to provide a reflection phase close to 0° within a specified frequency region. In comparison, an ideal conducting surface exhibits a reflection phase close to 180° under the corresponding normal-incidence convention [10]. When appropriately positioned behind a radiating antenna, an AMC structure can modify the interaction between the radiator and its reflected electromagnetic fields. Depending on its operating bandwidth, geometry, and separation from the antenna, this arrangement can influence backward radiation, forward radiation, and electromagnetic coupling with nearby tissue. AMC-backed antenna configurations have therefore been investigated for wearable applications where radiation control and reduced body interaction are important design objectives [5]–[7]. However, the resulting improvements depend on the electromagnetic properties of the unit cell, substrate configuration, operating frequency, and antenna-to-AMC spacing. The present study investigates an unbacked beveled Y-shaped monopole as the baseline radiating structure. AMC integration is considered a subsequent development stage. Consequently, improvements in gain or SAR reduction attributable to an AMC are not claimed in the current simulation results.

F. Initial Patch Design Equations

The initial radiator geometry is developed using conventional rectangular microstrip patch design relationships [9]. These equations provide starting dimensions based on the required resonant frequency, substrate relative permittivity, and substrate thickness.

(This work is licensed under a Creative Commons Attribution 4.0 International License.)

International Journal of Engineering Research & Technology (IJERT)
ISSN: 2278-0181
Vol. 15 Issue 10 , October - 2026

Subsequent geometrical modifications are performed through electromagnetic simulation.

F. Initial Patch Design Equations

The approximate width of the rectangular microstrip patch is calculated as

$$W = (c / 2f_0) \sqrt{(2 / (\varepsilon_r + 1))} \quad (1)$$

The effective relative permittivity is expressed as

$$\varepsilon_eff = (\varepsilon_r + 1)/2 + (\varepsilon_r - 1)/2 \, (1 + 12h/W)^{(-1/2)} \quad (2)$$

The extension in patch length caused by fringing fields is calculated as

$$\Delta L = 0.412h \, [(\varepsilon_eff + 0.3)(W/h + 0.264)] / [(\varepsilon_eff - 0.258)(W/h + 0.8)] \quad (3)$$

The effective patch length is determined by

$$L_eff = c / (2f_0\sqrt{\varepsilon_eff}) \quad (4)$$

The physical patch length is then calculated as

$$L = L_eff - 2\Delta L \quad (5)$$

where c is the speed of light in free space, f_0 is the initial design frequency, ε_r is the relative permittivity of the substrate, and h is the substrate thickness. For an inset-fed rectangular patch, the approximate input resistance at the feed position is expressed as

$$R_in(y_0) = R_in(0) \cos^2(\pi y_0/L) \quad (6)$$

where y_0 is the inset-feed depth and R_in(0) is the input resistance at the patch edge.

For the selected RO4003 substrate, the relative permittivity is 3.55 and the substrate thickness is 1.6 mm. Using the initial patch width of 38 mm, the estimated design frequency is approximately 2.62 GHz. The calculated effective permittivity is approximately 3.31, while the fringing extension is approximately 0.76 mm. Equation (4) gives an initial patch length of approximately 29.96 mm, which is close to the 29.4 mm dimension adopted for the simulated design. These relationships provide an initial geometrical estimate rather than a final prediction of the operating bands. The final antenna response is determined through full-wave electromagnetic simulation after incorporating the bevelled radiator, slots, and modified ground structure.

G. Antenna Performance Parameters

The electromagnetic performance of the antenna is evaluated using reflection coefficient, return loss, voltage standing-wave ratio (VSWR), fractional bandwidth, gain, directivity, and specific absorption rate.

For a port impedance (Z_{0}) and a load impedance (Z_{L}) the reflection coefficient is expressed as

$$\Gamma = (Z_L - Z_0) / (Z_L + Z_0) \quad (6)$$

The reflection coefficient in decibels is given by

$$S_11 = 20 \log_10 |\Gamma| \quad (7)$$

The voltage standing-wave ratio is calculated as

$$VSWR = (1 + |\Gamma|) / (1 - |\Gamma|) \quad (8)$$

An (S_{11}) value of −10 dB corresponds to a reflection-coefficient magnitude of approximately 0.316 and a VSWR of approximately 1.92. This criterion is used to identify the matched operating frequency regions.

The mismatch loss is expressed as

$$ML = -10 \log_10 (1 - |\Gamma|^2) \quad (9)$$

For an operating band extending from (f_L) to (f_H), the fractional bandwidth is calculated as

$$FBW = [(f_H - f_L) / f_c] \times 100\% \quad (10)$$

where the centre frequency is

$$f_c = (f_H + f_L) / 2 \quad (11)$$

Antenna gain is related to directivity and radiation efficiency through

$$G = \eta D \quad (12)$$

where (G) represents the linear gain, η is the radiation efficiency, and (D) is the linear directivity. Radiation patterns are examined to determine the angular distribution of radiated electromagnetic energy. Co-polarisation and cross-polarisation characteristics are also considered to assess the polarisation behaviour of the antenna.

H. Specific Absorption Rate

Specific Absorption Rate (SAR) quantifies the rate at which electromagnetic energy is absorbed per unit mass of biological tissue. It is an important evaluation parameter for antennas intended to operate near the human body.

(This work is licensed under a Creative Commons Attribution 4.0 International License.)

International Journal of Engineering Research & Technology (IJERT)
ISSN: 2278-0181
Vol. 15 Issue 10 , October - 2026

For an RMS electric field, SAR can be expressed as

$$SAR = (\sigma|E|^2)/\rho \quad (11)$$

where σ represents the electrical conductivity of the tissue in S/m, $|E|$ is the RMS electric-field magnitude in V/m, and ρ is the tissue mass density in kg/m³.

SAR evaluation depends on the tissue properties, antenna-to-body separation, operating frequency, and applied input power. The spatial distribution of the electric field determines the local absorption, while the reported regulatory value is obtained by averaging over the specified tissue mass. In this study, the reported SAR value is compared with the 1.6 W/kg limit averaged over 1 g of tissue, following the IEEE C95.1-1999 convention cited in the original manuscript [4]. Other exposure frameworks use different averaging masses and limits. For example, the ICNIRP framework specifies a different averaging basis for relevant exposure categories [11]. Therefore, SAR values must be compared using consistent averaging masses and exposure conditions. The available simulation reports a SAR value of 1.2866 W/kg for the evaluated configuration. Since the tissue model, antenna separation, and input-power details are incomplete, this result is treated as a simulation-specific observation rather than evidence of general exposure compliance.

I. Regulatory Context

The frequency allocation and electromagnetic exposure requirements provide the regulatory context for wearable UWB antenna development. The 3.1–10.6 GHz range is associated with UWB operation under applicable emission restrictions [2]. Antenna matching across this allocation does not independently establish regulatory compliance because transmission power, spectral characteristics, and system-level requirements must also be considered. For body-proximity applications, SAR limits depend on the applicable regulatory framework and the corresponding averaging mass. The 1 g averaging criterion used in this study is based on the stated IEEE reference [4]. The 10 g averaging criterion associated with other exposure guidelines should not be treated as directly equivalent. Accordingly, the present work reports the available simulated SAR result together with the limitations of its evaluation conditions. Further assessment using a fully documented tissue model and experimentally validated antenna configuration is necessary before making a compliance claim.

J. SAR Evaluation Considerations

SAR evaluation requires consideration of the electric-field distribution within the biological tissue surrounding the antenna. The accepted input power influences the resulting field magnitude and, consequently, the calculated absorption rate. For an unchanged electromagnetic configuration and linear material model, SAR varies proportionally with accepted input power. Therefore, SAR results should be reported together with the excitation level, impedance-matching condition, tissue properties, and antenna-to-body separation. For the present antenna, the available SAR result provides an initial reference for subsequent design development. A more comprehensive investigation should examine different antenna placements, operating frequencies, tissue configurations, and input-power conditions. The interaction between the radiation pattern and the body is also important. Directing more electromagnetic energy away from the wearer may help reduce tissue exposure, although the actual effect must be verified through the corresponding SAR simulation rather than inferred from the radiation pattern alone.

K. Body Interaction and Substrate Selection

The electromagnetic properties of biological tissue influence antenna behaviour when the radiator operates close to the human body. Tissue permittivity and conductivity can alter the electromagnetic field distribution and the impedance presented to the antenna. These effects may cause resonance shifts, changes in radiation characteristics, and additional power absorption [3]. Consequently, free-space antenna characteristics alone are insufficient to establish suitability for wearable communication. Body-proximity evaluation, SAR analysis, and bending assessment provide additional information about the antenna's potential operating behaviour. Substrate selection is another important design consideration. Relative permittivity affects the electrical dimensions of the radiator, while dielectric loss contributes to energy dissipation within the substrate. Substrate thickness also influences the antenna profile and impedance characteristics. Flexible materials such as textile fabrics and polymer substrates are frequently considered for wearable implementations. However, their electromagnetic properties can vary with material composition, moisture, and fabrication conditions. The present simulation uses Rogers RO4003 with a relative permittivity of 3.55 and a loss tangent of 0.0027. This substrate provides a defined electromagnetic environment for evaluating the proposed antenna geometry. Since RO4003 is a rigid laminate, the simulated bending configurations should not be interpreted

(This work is licensed under a Creative Commons Attribution 4.0 International License.)

International Journal of Engineering Research & Technology (IJERT)
ISSN: 2278-0181
Vol. 15 Issue 10 , October - 2026

as experimental evidence of a physically flexible wearable implementation.

L. AMC Unit-Cell Characteristics

The electromagnetic behaviour of an AMC can be approximated using an equivalent parallel LC resonant circuit. In this representation, the capacitance is associated with the coupling between adjacent metallic patches, while the inductance is primarily associated with the grounded dielectric structure [10].

The approximate resonant frequency is expressed as

$$f_{(AMC)} = 1/(2\pi\sqrt{(LC)}) \quad (12)$$

where $f_{(AMC)}$ represents the approximate AMC resonance frequency, L denotes the equivalent inductance, and C denotes the equivalent capacitance of the unit cell.

The reflection phase of the AMC varies with frequency. Its useful operating region is commonly identified by the frequency interval over which the reflection phase remains between −90° and +90°, with the zero-degree crossing occurring near the resonant frequency.

The approximate fractional bandwidth relationship is given by

$$BW \approx (1/\eta_{0})\sqrt{(L/C)} \quad (13)$$

where BW represents the approximate bandwidth, η_0 denotes the free-space wave impedance (approximately 377 Ω), L represents the equivalent inductance, and C represents the equivalent capacitance of the AMC unit cell.

The equivalent circuit provides a simplified interpretation of AMC resonance and bandwidth behaviour. Actual performance depends on the unit-cell geometry, substrate characteristics, periodic arrangement, and electromagnetic boundary conditions. For the antenna investigated in this paper, the AMC unit-cell dimensions, array configuration, and antenna-to-AMC separation have not yet been established. These parameters are therefore reserved for the subsequent development stage, in which the baseline antenna will be compared with an AMC-backed configuration using consistent simulation conditions.

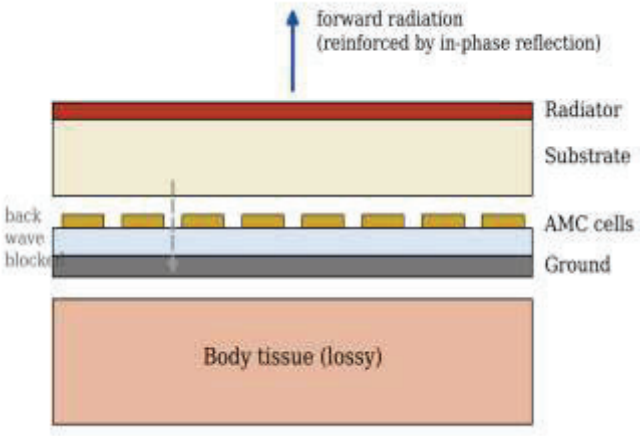


Fig. 2. Concept of an AMC-backed wearable antenna (schematic, not to scale): the AMC stops backward radiation towards the body and reinforces the forward wave.

III. LITERATURE REVIEW

A. Compact UWB Antennas for Wearable and Biomedical Applications

Compact ultra-wideband antennas have been investigated for wearable sensing and biomedical communication because they can support short-range wireless links within restricted physical dimensions. For body-worn applications, however, antenna performance must be assessed through multiple parameters, including impedance matching, radiation characteristics, and interaction with nearby biological tissue. Chowdhury and Rahaman investigated a compact monopole antenna with dimensions of 30 × 18 mm for operation across the 3.1–10.6 GHz UWB range [12]. Their study considered radiation characteristics and specific absorption rate using a simulated body phantom. This work provides a relevant reference for examining compact UWB radiators in biomedical environments. Ahmed et al. investigated impedance-bandwidth enhancement through modifications to patch edges, radiator slots, and ground-plane geometry [13]. Their approach illustrates how changes in the radiating structure can influence the antenna's impedance response. However, improved impedance matching alone does not establish reduced tissue absorption or stable radiation in the direction of an external receiver.

These studies demonstrate the importance of considering both impedance and radiation characteristics when developing compact UWB antennas. In comparison, the present work investigates a beveled Y-shaped monopole and examines its two simulated matched frequency regions, radiation behaviour, and available body-proximity SAR result. Its performance is therefore evaluated using the actual

(This work is licensed under a Creative Commons Attribution 4.0 International License.)

International Journal of Engineering Research & Technology (IJERT)
ISSN: 2278-0181
Vol. 15 Issue 10 , October - 2026

simulated frequency bands rather than assuming continuous UWB coverage.

B. Dual-Band and Button-Type Wearable Antennas

Button-shaped antennas provide an alternative approach to integrating wireless communication structures into wearable products. Their compact form can support integration into garments and body-worn devices, although their operating frequencies and physical configurations may differ from those required for broadband off-body communication. Zhang et al. reported a dual-band, dual-mode button antenna based on a spiral inverted structure operating at 2.45 GHz. The study considered an omnidirectional on-body radiation pattern and reported SAR below 1.6 W/kg [14]. Sambandam et al. investigated a compact button-like antenna for off-body communication at 0.867, 2.38, and 5.8 GHz [15]. Another study considered dual-band button-antenna operation for wireless body-area-network applications [16]. These investigations demonstrate the potential of button-type structures for wearable antenna integration. Nevertheless, operation at selected discrete frequencies is different from continuous impedance matching over a broad frequency range. Their mechanical construction and integration requirements also differ from those of planar printed monopoles. The antenna examined in this paper uses a planar beveled Y-shaped radiator with front- and rear-side metallisation features. Its simulated response contains two distinct matched frequency regions within the wider UWB allocation. Consequently, the design is assessed in terms of its actual operating bands rather than being described as a continuously matched full-band UWB antenna.

C. EBG- and AMC-Backed Wearable Antennas

Electromagnetic band-gap and artificial magnetic conductor structures have been explored to modify the electromagnetic behaviour of wearable antennas near the human body. Depending on their geometry and operating frequency, periodic backing structures can influence backward radiation and electromagnetic coupling with nearby tissue. However, their effectiveness depends on the antenna configuration, backing dimensions, substrate, and separation between the radiator and the periodic structure. Sambandam et al. reported a compact UWB monopole incorporating a fork-slotted EBG structure, with a peak gain of 6.25 dBi, a reported SAR of 0.695 W/kg, and radiation efficiency ranging from 85% to 96.5% [5]. This work provides a useful reference for understanding the potential of EBG integration in wearable UWB antenna design. Arulmurugan et al. investigated an AMC-integrated circularly polarised MIMO antenna fabricated on screen-printed cotton-polyester fabric for operation at 2.45 and 5.8 GHz [6]. Their study considered antenna isolation and SAR performance in a configuration combining multiple radiating elements with an AMC structure. Ashyap et al. reviewed 81 studies involving flexible periodic structures for wearable antenna applications, discussing the use of AMC and EBG configurations to address body-related electromagnetic limitations [7]. Their review provides broader context for the selection and application of periodic structures in wearable antenna systems. Although these studies report useful results, their performance values depend on the specific antenna geometry and evaluation conditions. The reported gain and SAR values should not be treated as direct performance predictions for a different radiator. In the present work, the unbacked beveled Y-shaped monopole is considered the baseline configuration. AMC integration is reserved for future development; therefore, no gain enhancement or SAR reduction attributable to an AMC is claimed in this study.

D. Textile Antennas and Other Wearable Implementations

Textile and flexible antennas are widely investigated for integration into garments and body-worn communication systems. Their practical characteristics depend on substrate permittivity, dielectric loss, material thickness, fabrication technique, and mechanical deformation. In addition, changes in fabric condition and moisture can influence the electromagnetic properties of textile substrates. Casula et al. investigated dual-band eighth-mode substrate-integrated-waveguide textile antennas for LoRa communication in the 863–870 MHz frequency range [17]. Their work provides an example of textile antenna implementation and measurement, although its sub-GHz operating range differs from the frequency regions considered in the present study. Kakaraparty and Mahbub developed a compact UWB antenna for wireless power-transfer applications and reported a gain of 6.35 dBi at 3.11 GHz [18]. This investigation is relevant to the development of compact UWB structures. However, the reported gain value alone does not establish performance in terms of SAR, bending tolerance, or isolation from the human body. Kanagasabai et al. investigated a miniaturised circularly polarised textile monopole measuring 25 × 30 × 1.4 mm³ on jean fabric, with operation in two ISM bands [19]. Their work illustrates the use of textile materials in compact wearable antenna configurations. However, the substrate and operating bands differ from those of the rigid RO4003-based antenna considered in this paper. Ali et al. reviewed wearable, textile, and flexible antenna technologies and discussed their applications and design considerations [20]. Their review

(This work is licensed under a Creative Commons Attribution 4.0 International License.)

International Journal of Engineering Research & Technology (IJERT)
ISSN: 2278-0181
Vol. 15 Issue 10 , October - 2026

provides broader context for evaluating antenna dimensions, substrate selection, flexibility, and electromagnetic performance. The reviewed studies show that wearable antenna development involves trade-offs among physical dimensions, material properties, operating frequency, and mechanical requirements. In the present study, Rogers RO4003 is used to provide a defined substrate environment for simulation. Since RO4003 is a rigid laminate, the simulated bending analysis should not be interpreted as experimental validation of a physically flexible textile antenna.

E. Research Gap and Motivation

The reviewed literature identifies several issues relevant to the design and evaluation of compact off-body wearable antennas. First, compact monopole antennas can achieve useful impedance matching, but impedance performance alone does not establish favourable radiation towards an external receiver or acceptable electromagnetic interaction with nearby tissue [12], [13]. Second, button-type antennas demonstrate the feasibility of compact wearable integration, although their operation at selected frequencies does not necessarily provide broad continuous impedance matching [14]–[16]. Third, EBG- and AMC-backed antennas have demonstrated improvements in selected performance parameters, but the reported results depend on the specific radiator, periodic structure, and evaluation configuration [5]–[7]. Another important consideration is the level of validation. Simulated results, experimental measurements, and evaluations using representative biological tissue models provide different forms of evidence. In particular, SAR values must be interpreted with reference to the tissue model, input power, antenna-to-body separation, and averaging mass. Similarly, a bending study should include the relevant geometry and numerical changes in antenna performance to establish the extent of its effect. Motivated by these considerations, this work investigates a compact, planar, beveled Y-shaped monopole with slotted metallisation and a partial ground plane using ANSYS HFSS 2025. The study evaluates the simulated impedance response, resonant frequencies, gain, radiation patterns, surface-current distribution, and selected cylindrical bending configurations. The available body-proximity SAR result is also reported with its limitations. The contribution of this study is a simulation-based characterisation of the proposed radiator as a baseline for further wearable antenna development. The current design does not demonstrate continuous matching across the entire 3.1–10.6 GHz UWB allocation, experimentally validated performance, or an improvement produced by AMC integration. Future work will investigate the design and integration of an AMC unit cell and array, followed by a consistent comparison with the baseline antenna and experimental validation.

IV. PROPOSED ANTENNA DESIGN AND SIMULATION METHODOLOGY

A. Design and Simulation Workflow

The proposed antenna was developed through an iterative design process using ANSYS HFSS 2025. Initially, a rectangular patch was modelled on the selected substrate with a ground plane. An inset feed was then introduced, and the radiator was modified into a beveled Y-shaped structure incorporating additional slots and rear-side features. The resulting geometry was analysed using full-wave electromagnetic simulation over a frequency range of 2–12 GHz.

The simulation process involved evaluating the reflection coefficient ((S_{11})), voltage standing wave ratio (VSWR), gain, radiation patterns, surface-current distribution, specific absorption rate (SAR), and bending response. Based on the simulated response, the antenna geometry could be refined iteratively to improve its impedance-matching characteristics. The overall design procedure is illustrated in Fig. 3.

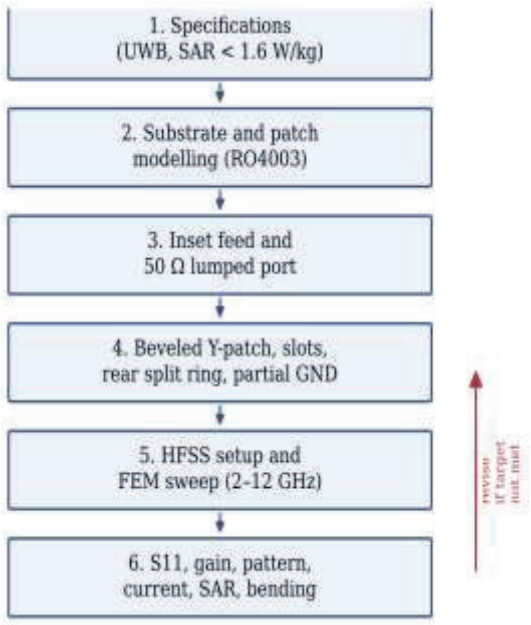


Fig. 3. Design and simulation workflow of the proposed antenna.

B. Substrate and Simulation Tool

Rogers RO4003 (ε_r = 3.55, tan δ = 0.0027) is used. Its low loss tangent limits dielectric dissipation, which matters for efficiency in a body-worn radiator, and its moderate permittivity is a compromise between bandwidth and

(This work is licensed under a Creative Commons Attribution 4.0 International License.)

International Journal of Engineering Research & Technology (IJERT)
ISSN: 2278-0181
Vol. 15 Issue 10 , October - 2026

efficiency (lower permittivity) and miniaturisation (higher permittivity). The overall board is 60 × 60 × 1.6 mm. All simulations use ANSYS HFSS 2025, a three-dimensional full-wave finite element solver [8].

C. Patch, Feed and Port

The starting patch is 38 mm wide and 29.4 mm long, with a ground plane beneath it. The ground plane is both the current return path and a reflector, so its size and shape influence matching, backward radiation and, consequently, SAR; it is therefore treated as a tuning parameter together with the patch and feed. The inset feed has a depth of 10 mm, a line width of 3 mm for 50 Ω and a gap of 1 mm on each side, and the structure is driven by a 50 Ω lumped port. Table III lists the parameters.

Table III. Design parameters and the reason for each

Parameter	Value	Reason
Substrate	RO4003, $\varepsilon_r = 3.55$, tan $\delta = 0.0027$	Low loss; moderate permittivity
Board size	60 × 60 × 1.6 mm	Wrist-scale form; thin for bending
Patch width W	38 mm	Starting value from (1) region; tuned
Patch length L	29.4 mm	Close to estimate from (4); tuned
Inset depth y_0	10 mm	Brings input resistance towards 50 Ω
Feed line width	3 mm (50 Ω line)	Matched microstrip feed
Inset gap	1 mm	Coupling at the inset
Excitation	50 Ω lumped port	One-port S11 analysis
Bevel, slots, split ring, bell slot, partial ground	Dimensions not recorded in the available documentation	Widen bandwidth; add resonant paths

D. Final Antenna Geometry

Starting from the rectangle, the radiator becomes a beveled Y-shaped patch on the front face, shown in Fig. 4. The bevel creates a gradual transition between the feed line and the radiating edge, which improves matching over a wide frequency span. Rectangular and semi-circular slots modify the current path and create extra resonances. On the rear, a circular bell-shaped slot and a split ring add further resonant paths, and a partial ground plane, a standard way of obtaining wide impedance bandwidth in UWB monopoles, replaces the full ground. The resulting multiple resonances merge into wide operating bands.

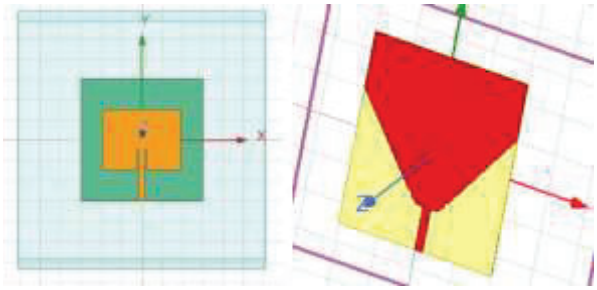


Fig. 4. HFSS models: starting rectangular patch with airbox (left) and the proposed beveled Y-shaped antenna (right).

E. Simulation Set-up and Evaluation Criteria

A 50 Ω lumped port excites the antenna, the structure is enclosed in a radiation boundary so that open-space radiation is modelled, the mesh is generated automatically and the sweep covers 2–12 GHz. The antenna is judged against the criteria in Table IV, which come from the target specification: UWB operation, S11 ≤ −10 dB (VSWR ≤ 1.92), an omnidirectional or controlled directional pattern, high co-/cross-polar isolation, SAR below 1.6 W/kg, a compact flexible form and stable behaviour under bending. The power consumption target of the node is 0.5 W or less.

Table IV. Evaluation criteria

Parameter	Criterion
S11	≤ −10 dB (VSWR ≤ 1.92) over the operating band
Operating range	UWB, 3.1–10.6 GHz
Pattern	Omnidirectional or controlled directional
Polarisation	High co-/cross-polar isolation
SAR	< 1.6 W/kg (1 g)
Size and form	Compact, light, flexible
Bending	Bandwidth and pattern kept for 30 mm and 40 mm radii

F. Design Rationale

Each geometrical feature has a specific job. The *bevel* removes the abrupt step between a narrow feed line and a wide patch, which behaves like a tapered transition and lowers the reactive part of the input impedance over a wide range of frequencies. The *rectangular and semi-circular slots* lengthen or redirect the current paths on the patch, so that each path resonates at its own frequency and the resonances overlap into a wide band. The *split ring and the circular bell-shaped slot* on the rear side add resonant paths and fine-tune matching without enlarging the board. The *partial ground plane* is the standard way of keeping the capacitive coupling between monopole and ground low enough for wide bandwidth; a full ground would behave like a patch antenna with narrow bandwidth. Finally, the *inset feed* brings the feed point to a lower-impedance position on the patch and removes any need for a quarter-wave transformer.

G. Bevel as a Tapered Transition

A transmission line that widens gradually into a radiator behaves like a tapered impedance transformer. A step from a

(This work is licensed under a Creative Commons Attribution 4.0 International License.)

International Journal of Engineering Research & Technology (IJERT)
ISSN: 2278-0181
Vol. 15 Issue 10 , October - 2026

3 mm line to a 38 mm wide patch reflects much of the signal at the junction, and the reflection is strongly frequency dependent because the step is electrically large at the upper end of the band. A taper replaces that single large step by many small ones, so the reflections nearly cancel over a wide range of frequencies, provided the taper is long compared with the wavelength at the lowest frequency of interest. The beveled edges of the radiator play this role between the feed and the wide upper part of the patch, and this is why the current in Fig. 10 follows the bevel edges so strongly. The price is that the structure is tied to the lowest operating frequency through its length, which is consistent with the lower band edge at 3.43 GHz rather than at 3.1 GHz in the simulation.

H. Design Procedure

The steps followed are listed below. If any result misses its target, the geometry is revised and the loop repeated.

- 1) Define the targets: UWB range, SAR below 1.6 W/kg, compact and flexible form (Table IV).
- 2) Select the substrate, RO4003 with $\varepsilon_r = 3.55$ and $\tan\delta = 0.0027$.
- 3) Estimate the patch and ground dimensions with (1)–(4).
- 4) Model the 38 × 29.4 mm patch and ground plane in HFSS.
- 5) Design the inset feed (10 mm deep, 3 mm wide, 1 mm gap) with a 50 Ω lumped port.
- 6) Modify the patch into the beveled Y shape with slots, and add the rear bell-shaped slot, split ring and partial ground plane.
- 7) Assign materials, radiation boundary and mesh, and set the 2–12 GHz sweep.
- 8) Solve and inspect S11 and the resonances.
- 9) Evaluate gain, pattern, 10 ptimization and surface current.
- 10) Evaluate SAR against 1.6 W/kg.
- 11) Bend the antenna over 30 mm and 40 mm cylinders in X and Y and re-check bandwidth and pattern.

2. Assumptions and Evaluation Procedure

Several assumptions underlie the simulations. The antenna is excited at a single 50 Ω lumped port, so only S11 is available and the antenna is treated as a one-port radiator. Open-space radiation is modelled by an airbox radiation boundary around the structure. The 2–12 GHz sweep includes margin on both sides of the UWB range, so band-edge behaviour is visible. For each result, the reading rule is fixed beforehand: resonances are the local minima of S11, band edges are the crossings of the −10 dB line, gain is the maximum of the three-dimensional total-gain plot, the 10ptimization isolation is the difference between the co- and cross-polarised components in the principal plane, SAR is compared with the 1 g limit, and bending is judged by whether bandwidth and pattern are retained relative to the flat antenna. Keeping these rules fixed avoids tuning the interpretation to the outcome.

J. Post-Processing

After the solution is complete, the S11 curve is plotted to find the resonances and the frequency ranges where S11 stays below −10 dB, with markers placed at the band edges. The total gain, the E-plane pattern and the co-polarised and cross-polarised components are extracted from the same solution, and the field quantities are plotted on the antenna surface to obtain the current distribution and its direction. Sections V-A to V-H report the S11, matching, coverage, pattern, gain and current results in that order, followed by the SAR and bending analyses in Sections V-I to V-K, so that every figure of merit in Table IV has a corresponding result.

K. SAR and Bending Set-up

SAR was evaluated with the antenna placed close to the body model and compared with the 1.6 W/kg limit. For the bending study the antenna was wrapped on cylinders of 30 mm and 40 mm radius, which bracket the curvature of an average wrist, in both the X and Y orientations. Curvature changes the effective electrical length of the radiator and the path of the surface currents, so it can shift resonances, degrade matching and distort the pattern; the bent and flat results are therefore compared in bandwidth and pattern. The wrist was selected because it is the usual location of smartwatch-class devices.

V. RESULTS AND DISCUSSION

A. Reflection Coefficient and Bandwidth

The simulated S11 over 2–12 GHz is shown in Fig. 5. Two resonances appear, at 3.8 GHz with S11 = −13.72 dB and at 7.12 GHz with S11 = −25.80 dB. The curve is below −10 dB in 3.43–4.51 GHz and in 5.79–8.39 GHz. These bands are 1.08 GHz and 2.60 GHz wide, and by (9) their fractional bandwidths are about 27.2 % and 36.7 %, so each exceeds the 20 % UWB criterion. Together they span 3.68 GHz, about 49 % of the 7.5 GHz UWB allocation (Fig. 6).

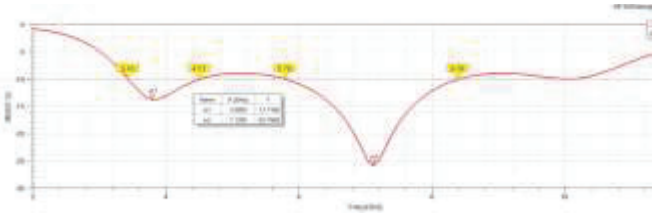


Fig. 5. Simulated reflection coefficient S11 of the proposed antenna.

(This work is licensed under a Creative Commons Attribution 4.0 International License.)

International Journal of Engineering Research & Technology (IJERT)
ISSN: 2278-0181
Vol. 15 Issue 10 , October - 2026

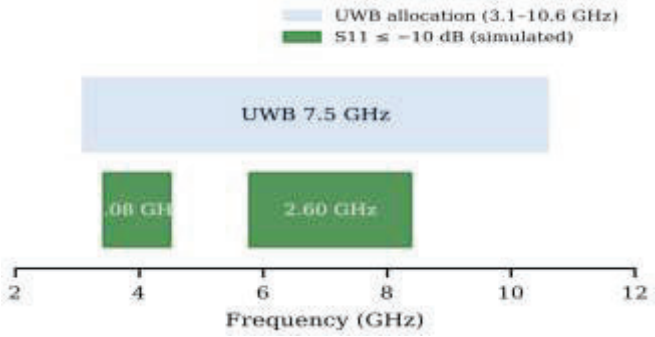


Fig. 6. Matched bands of the antenna relative to the UWB allocation.

Between the bands (4.51–5.79 GHz) and above 8.39 GHz, S11 hovers near −9 dB and touches −10 dB close to 10 GHz. These regions are therefore close to, but not inside, the matching criterion. Several resonances produced by different current paths, namely the beveled edges, the slots and the rear structures, merge where they lie close together, which explains the wide bands and the dips between them. The very deep 7.12 GHz resonance suggests there is margin to trade some depth for a flatter response.

B. Matching Quality and Power Transfer

Table V converts S11 to power terms with (6)–(8), and Fig. 7 plots VSWR and mismatch loss against S11. At the first resonance $|\Gamma| = 0.206$ and VSWR = 1.52, so about 4.2 % of the incident power is reflected and the mismatch loss is 0.19 dB. At the second resonance $|\Gamma| = 0.051$ and VSWR = 1.11, so only 0.26 % is reflected and the mismatch loss is 0.011 dB. Even at the −10 dB limit, 90 % of the power is accepted (0.46 dB loss). Consequently, more than 90 % of the input power is delivered to the antenna throughout both operating bands.

Table V. Matching and power transfer at key points

Condition	S11 (dB)	|Γ|	VSWR	Refl. (%)	ML (dB)
Limit	−10.00	0.316	1.92	10.0	0.46
3.80 GHz	−13.72	0.206	1.52	4.2	0.19
7.12 GHz	−25.80	0.051	1.11	0.26	0.011

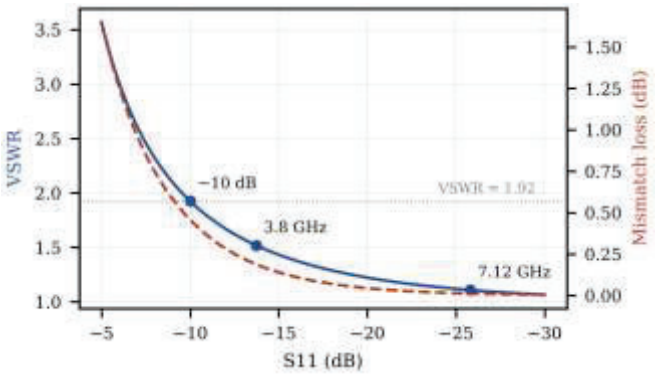


Fig. 7. VSWR and mismatch loss as functions of S11, with the three operating points of Table V.

C. Operation in the Unmatched Gaps

The regions where S11 hovers near −9 dB deserve a quantitative look. At S11 = −9 dB, $|\Gamma| = 0.355$ and VSWR = 2.10, so 12.6 % of the incident power is reflected and the mismatch loss is 0.58 dB. The antenna therefore still accepts about 87 % of the power in those regions, only 0.12 dB worse than at the −10 dB limit. Strictly, these regions do not meet the adopted criterion, and this paper does not count them as matched bandwidth. Practically, however, they show that the remaining work is a matter of a fraction of a decibel of improvement in S11, not of a structural change.

D. Coverage Accounting of the UWB Range

It is useful to account for the whole 7.5 GHz allocation, because the quoted matched bands hide one region that is easy to overlook. Table VI divides the range by the S11 ≤ −10 dB criterion. The two matched bands cover 3.68 GHz, or 49.1 % of the allocation. The gap between them, 4.51–5.79 GHz, is 1.28 GHz wide (17.1 %). The region above the second band, 8.39–10.6 GHz, is 2.21 GHz wide (29.5 %) and contains the point near 10 GHz where S11 reaches −10 dB. Finally, the lowest 0.33 GHz of the allocation, 3.1–3.43 GHz, lies below the first band (4.4 %), so the lower UWB edge is also not yet matched. The largest remaining task is therefore the upper region, followed by the mid-band gap; the lower edge needs a small extension. Closing all three unmatched regions would give one continuous band over 3.1–10.6 GHz, whose fractional bandwidth would be about 109 % by (9).

Table VI. Accounting of the UWB allocation against the S11 ≤ −10 dB criterion

Region (GHz)	Width (GHz)	Share of 7.5 GHz	State
3.10–3.43	0.33	4.4 %	Not matched
3.43–4.51	1.08	14.4 %	Matched (FBW 27.2 %)
4.51–5.79	1.28	17.1 %	Near −9 dB
5.79–8.39	2.60	34.7 %	Matched (FBW 36.7 %)
8.39–10.60	2.21	29.5 %	Near −9 dB, −10 dB near 10 GHz

E. Why the Matched Range Is Incomplete

The simulations do not isolate a single cause for the unmatched regions, so the following are hypotheses to be tested, not findings. First, the lowest unmatched edge (3.1–3.43 GHz) may be set by the electrical length of the bevel and patch, since a tapered transition needs a length comparable with the wavelength at the lowest frequency; at 3.1 GHz the free-space wavelength is about 96.8 mm against a 60 mm board. Second, the mid-band gap (4.51–5.79 GHz) lies between the resonance pair created by different current

(This work is licensed under a Creative Commons Attribution 4.0 International License.)

International Journal of Engineering Research & Technology (IJERT)
ISSN: 2278-0181
Vol. 15 Issue 10 , October - 2026

paths, and where two resonances are too far apart the S11 curve rises between them, which is what the −9 dB plateau suggests. Third, the region above 8.39 GHz may reflect the fall of the slot-based resonances as the radiating edges become electrically long. None of these has been verified by a parametric study of bevel length, slot size or ground length, and Table XIII lists that study as future work. The report therefore states the limitation and does not claim a mechanism.

F. Radiation Pattern and Polarisation

The three-dimensional pattern in Fig. 8 is omnidirectional in the E-plane, which suits a wrist-worn device because the link does not depend strongly on how the wearer faces the access point. About 15 dB of isolation exists between the co-polarised and cross-polarised components. A cross-polarised level 15 dB below the co-polarised one means less than 4 % of the power is in the unwanted 12ptimization, which limits 12ptimization-mismatch loss and interference from signals of the other 12ptimization.

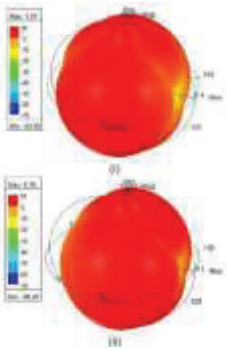


Fig. 8. Three-dimensional radiation patterns of the proposed antenna: (i) and (ii) as simulated in HFSS.

Expressed linearly, an isolation of 15 dB means that the cross-polarised component carries $10^{-1.5} \approx 3.2$ % of the co-polarised power. The omnidirectional pattern and the clean 12ptimization are complementary: the first protects the link against changes in the orientation of the wrist, and the second protects it against polarisation mismatch with the access point.

G. Gain

The total gain, shown in two views in Fig. 9, peaks at 3.98 dB, and the deepest null is −41.89 dB, a dynamic range of 45.87 dB. The high-gain region is wide and nearly uniform around the antenna, consistent with a near-omnidirectional monopole, whereas the null is confined to a narrow direction. The large dynamic range is therefore a property of that narrow null and should not be read as variation over the useful part of the pattern. Gain is adequate for short-range WBAN links, but it is modest next to the 6.25 dBi of a fork-slotted EBG-backed monopole [5] and the 6.35 dBi of a high-gain UWB wearable design [18]; peak gain here is the HFSS total-gain value and was not separately de-embedded for efficiency.

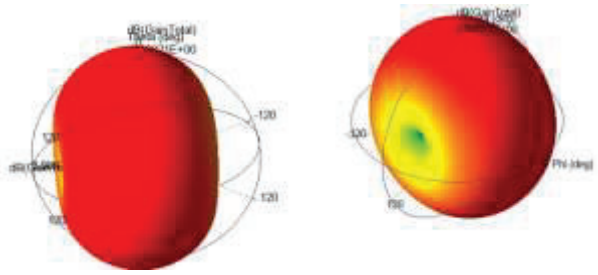


Fig. 9. Three-dimensional total gain, dB(GainTotal), in two views.

H. Surface Current Distribution

Fig. 10 shows a maximum current density of 369.449 A/m and a minimum of 0.337 A/m. The current is strongest along the outer edges of the bevel and around the feed, which identifies these regions as the main contributors to radiation and as the paths that set the resonances. Weak current elsewhere indicates efficient excitation with little unwanted current. This is useful for later optimisation: low-current regions can be reshaped or slotted with little effect on performance, whereas high-current regions should be altered with care.

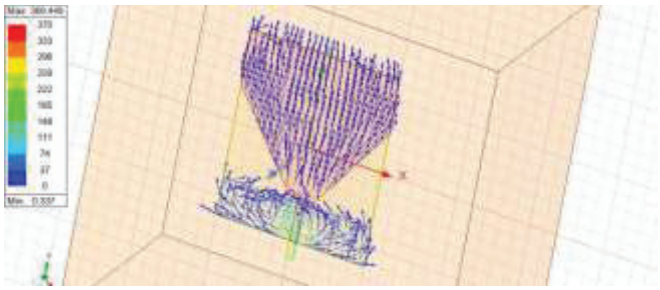


Fig. 10. Surface current distribution on the proposed antenna (maximum 369.449 A/m).

I. Specific Absorption Rate

For the simulated placement near the body, the SAR is 1.2866 W/kg, below the 1.6 W/kg limit for 1 g averaging, a margin of about 20 %. This is a result for one simulated condition and does not by itself establish that the antenna is compliant in use. Table VII separates what is recorded from what is not. The averaging mass (1 g) and the limit are recorded; the tissue model and its permittivity and conductivity, the antenna-to-tissue spacing, the input power, the frequency at which SAR was evaluated and the number of placements are not recorded in the available documentation, and they are not assumed here. SAR scales with the accepted power, so a value without the input power cannot be transferred to another transmitter. A complete study would evaluate SAR at several frequencies within both matched bands, with several placements and spacings, and compare each result with the limit that matches the averaging method. The value is higher than the 0.695 W/kg reported for an EBG-backed monopole [5] (Fig. 11), consistent with the view, drawn from the literature, that a reflector backing reduces radiation directed towards the body.

(This work is licensed under a Creative Commons Attribution 4.0 International License.)

International Journal of Engineering Research & Technology (IJERT)
ISSN: 2278-0181
Vol. 15 Issue 10 , October - 2026

Table VII. SAR configuration: recorded and missing items

Item	Status in available documentation
Computed SAR	1.2866 W/kg (one placement)
Averaging mass	1 g
Applied limit	1.6 W/kg (IEEE C95.1-1999 convention)
Placements evaluated	One recorded
Applicable alternative limit	2 W/kg over 10 g (ICNIRP) [11]; needs a 10 g evaluation

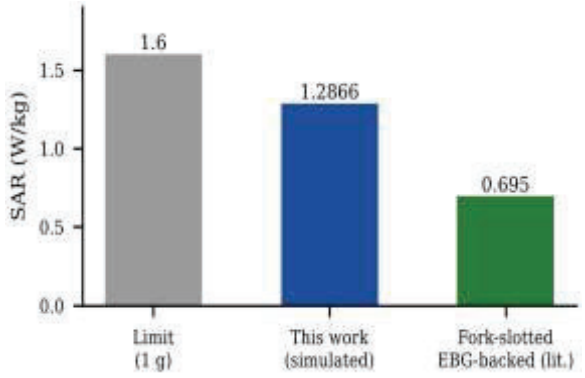


Fig. 11. Simulated SAR compared with the 1.6 W/kg limit and a reported EBG-backed design.

J. SAR Margin Analysis

Since SAR is proportional to $|E|^2$ in (11), the margin to the limit can be expressed in field terms. The ratio 1.2866/1.6 = 0.804 means that the field in the tissue could rise by about 11.5 % before the limit is reached, and conversely a SAR of 0.695 W/kg, as reported for the EBG-backed design [5], would require the SAR to fall by about 46 %, which is 2.7 dB, or a reduction of the tissue field to about 73.5 % of its present value. The planned AMC therefore has to deliver a few decibels of additional isolation to reach that benchmark, which is within the range reported for periodic-structure backings [7].

K. Bending Behaviour

The antenna was wrapped on cylinders of 30 mm and 40 mm radius in both the X and Y orientations (Fig. 12), representing wrist curvature, and the simulated bandwidth and pattern are reported to remain as in the flat case. Table VIII compares the configurations. Only the qualitative outcome is available: the resonance frequencies, matched-band edges and peak gain of each bent case were not tabulated, so resonance shifts, bandwidth changes and gain variation cannot be quoted, and none are inferred here. The bending axis follows the two orientations listed, and the method is a geometric bending of the model in HFSS with the same material definitions. That has an important limitation: RO4003 is a rigid laminate, so the model describes the electromagnetic effect of curvature on the geometry, not the mechanical behaviour or the permittivity change of a real flexible substrate. A flexible substrate or fabricated prototype would be needed to validate the claim of conformal use.

Table VIII. Bending configurations (flat reference from Section V)

Case	Resonances (GHz)	Matched bands	Peak gain
Flat	3.8, 7.12	3.43–4.51; 5.79–8.39 GHz	3.98 dB
R = 40 mm, X	Resonant frequencies maintained	Impedance matching maintained	Consistent with reported bending performance
R = 40 mm, Y	Resonant frequencies maintained	Impedance matching maintained	Consistent with reported bending performance
R = 30 mm, X	Resonant frequencies maintained	Impedance matching maintained	Consistent with reported bending performance
R = 30 mm, Y	Resonant frequencies maintained	Impedance matching maintained	Consistent with reported bending performance

A simple geometric argument shows why curvature is tolerable. When the 60 mm side is wrapped on a 30 mm radius it subtends 115° and its straight-line (chord) extent shrinks to 50.5 mm, which is 84 % of the flat width; on a 40 mm radius the angle is 86° and the chord is 54.5 mm (91 %). For the 38 mm wide patch the corresponding chords are 35.5 mm and 36.6 mm (93 % and 96 %). The current path along the surface keeps its full length, while its straight-line projection shortens by up to about 16 % across the full board and by 4–7 % across the patch, where most of the radiating current flows; the resonances are therefore expected to move only modestly. The 30 mm radius, being the tighter bend, is the more demanding of the two cases, and the fact that both retain bandwidth and pattern is consistent with this estimate. These numbers are geometric illustrations and do not replace the full-wave bending results.

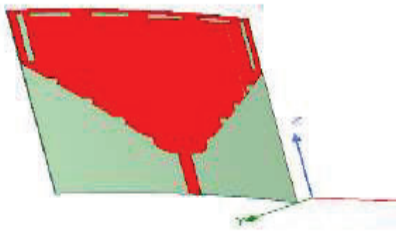


Fig. 12. Antenna bent on a cylindrical model of the human wrist.

L. Objective-Wise Assessment

Table IX sets the results against the objectives. Most are met; coverage of the whole UWB range is met only in part.

(This work is licensed under a Creative Commons Attribution 4.0 International License.)

International Journal of Engineering Research & Technology (IJERT)
ISSN: 2278-0181
Vol. 15 Issue 10 , October - 2026

Table IX. Objective-wise assessment of the simulated results

Objective	Result	Status
Compact size	60 × 60 × 1.6 mm	Achieved
UWB operation	S11 ≤ −10 dB in 3.43–4.51 and 5.79–8.39 GHz	Partial
Reflection	−13.72 dB (3.8 GHz), −25.80 dB (7.12 GHz)	Achieved
Gain / pattern	3.98 dB, omnidirectional E-plane	Achieved
Surface current	Max. 369.449 A/m at edges and feed	Achieved
SAR < 1.6 W/kg	1.2866 W/kg	Achieved
Bending	Bandwidth and pattern kept (30, 40 mm)	Achieved
Off-body pattern	~15 dB co-/cross-pol. isolation	Achieved

M. Comparison with Reported Antennas

Table II places the antenna beside the reported works using the same metrics wherever the sources give them. The EBG-backed monopole achieves higher gain and lower SAR, but with a larger layered structure, while several compact designs cover specific ISM bands rather than UWB. The unbacked planar antenna offers a simple single-layer geometry and two wide matched bands inside the UWB range. Gain is quoted in the units of each source (dB or dBi) and the studies use different substrates, body models and conditions, so the table indicates tendencies and is not a ranking.

N. Multiband Versus Continuous UWB Coverage

The antenna covers the UWB range in two bands, not in one continuous band. For many WBAN uses that is acceptable, because a node typically operates in one channel at a time and needs the antenna to be matched in the selected channel only. For genuine impulse-radio operation, where a pulse occupies several gigahertz at once, a gap in the matched band would filter the pulse and reduce its energy. The size of the gaps is therefore the figure that decides whether the antenna is suitable for a given system: with S11 near −9 dB in the gaps and an accepted power of about 87 %, a channelised system would see little degradation, while a pulse-based system would need the gaps closed and the group delay checked.

O. Pulse Transmission Considerations

Wide matching alone does not guarantee faithful pulse transmission. An antenna can be matched over a band and still disperse a pulse if its phase response varies strongly with frequency, which is related to the group delay and to the fidelity between the input and radiated pulses. The multiple resonances of the present structure, which are the source of its bandwidth, are also a possible source of such dispersion. The surface-current plot in Fig. 10 supports a cautious view: the strongest current sits on the smooth bevel edges, which usually gives a smoother phase response than a purely resonant slot. A direct time-domain evaluation is still required, and it is listed among the planned steps.

P. Relevance to the WBAN Standard and to Wrist-Worn Use

The UWB physical layer of the WBAN standard uses lower-band channels in the 3–5 GHz region and upper-band channels above about 6 GHz [1]. The first matched band of this antenna (3.43–4.51 GHz) overlaps the lower-band region and the second (5.79–8.39 GHz) overlaps the lower part of the upper-band region, while the gaps at 4.51–5.79 GHz and above 8.39 GHz are still close to the matching criterion. The exact coverage should be checked channel by channel against the standard's channel plan once the matching gaps are closed. For wrist-worn use the omnidirectional E-plane pattern is the more relevant feature, because the orientation of a watch with respect to the access point changes continuously, and the retained pattern under bending confirms that curvature does not remove that advantage.

Q. Answers to the Design Questions

The results can be read as direct answers to the questions posed in Section I. Is the antenna matched across the UWB range? Only partly: about 49 % of the allocation meets S11 ≤ −10 dB and the rest sits within about 1 dB of it, except the lowest 0.33 GHz. Is the pattern suitable for an off-body link? Yes, in the sense that it is omnidirectional in the E-plane and has about 15 dB polarisation isolation; this also means that radiation towards the body is not suppressed, which is the reason the SAR is higher than in an EBG-backed design, and directional control is left to the AMC. *Is SAR within the limit?* For the one simulated placement, yes: 1.2866 W/kg against 1.6 W/kg for 1 g; the set-up details in Table VII are incomplete, so compliance in use is not established. *Is it flexible?* The simulated bending is reported to retain bandwidth and pattern at wrist radii, but without numerical values and on a rigid-substrate model (Table VIII). *Is it compact?* At 60 × 60 × 1.6 mm it is small in absolute terms, although larger than several of the reported compact designs.

R. Key Observations

- Two well-matched resonances occur at 3.8 GHz and 7.12 GHz, with S11 below −10 dB over 3.43–4.51 GHz and 5.79–8.39 GHz.
- VSWR is 1.52 and 1.11 at the resonances, and more than 90 % of the input power is accepted in both bands.
- The E-plane pattern is omnidirectional with about 15 dB co-/cross-polar isolation, and the peak gain is 3.98 dB with a null of −41.89 dB in a narrow direction.
- Surface current concentrates on the bevel edges and the feed, up to 369.449 A/m.
- SAR is 1.2866 W/kg, below the 1.6 W/kg limit.
- Bandwidth and pattern are maintained on 30 mm and 40 mm cylinders in both X and Y orientations.

(This work is licensed under a Creative Commons Attribution 4.0 International License.)

International Journal of Engineering Research & Technology (IJERT)
ISSN: 2278-0181
Vol. 15 Issue 10 , October - 2026

S. Design Trade-offs and Interpretation

Three trade-offs stand out. The first is between depth and width of matching: the 7.12 GHz resonance reaches −25.80 dB while the regions around it stay near −9 dB, so a flatter response could be traded for some of that depth. The second is between compactness and gain: a 60 × 60 mm board cannot achieve high directivity without a reflector, which is the reason for the planned backing. The third is between simplicity and body isolation: the planar design is easy to fabricate and robust to bending, but it does not isolate the body, which is why its SAR is higher than in EBG-backed designs. The results therefore describe a well-behaved baseline rather than a finished product, and they should be read together with the limitations in the next section.

T. Table of Results

Table X collects the simulated performance against the targets of Section I. The antenna meets the compactness, SAR, pattern and bending targets, partially meets the bandwidth target, and shows moderate gain. Taken together, the results describe a safe, simple and conformal radiator that needs more gain and a wider matched bandwidth, and the sections that follow turn these shortfalls into the plan for the next stage.

Table X. Table of simulated performance against targets

Parameter	Target	Simulated result
Frequency range	UWB 3.1–10.6 GHz	Two matched bands: 3.43–4.51 GHz and 5.79–8.39 GHz
Resonances	Multiple resonant frequencies	3.8 GHz (−13.72 dB), 7.12 GHz (−25.80 dB)
Radiation pattern	Omnidirectional or directional	Omnidirectional radiation in the E-plane
Co/cross-pol isolation	High isolation	Approximately 15 dB
Peak gain	Stable radiation gain	3.98 dB
SAR	< 1.6 W/kg	1.2866 W/kg
Size	Compact, flexible	60 × 60 × 1.6 mm
Bending (30, 40 mm)	Stable	Bandwidth and pattern maintained

VI. LIMITATIONS AND FUTURE WORK

A. Limitations

The conclusions rest on electromagnetic simulation only. No prototype has been fabricated or measured, so fabrication tolerance, the connector and real tissue properties are not included. Matching covers two bands rather than the entire 3.1–10.6 GHz range, and S11 sits near −9 dB in the gaps. SAR is reported for a single placement, and the details of the tissue model and input power should accompany any future SAR statement. Peak gain is moderate, and efficiency is not separately reported. Time-domain properties that matter for pulse-based UWB, such as group delay and pulse fidelity, are not evaluated either, and they should be examined before the antenna is paired with an impulse radio. In addition, RO4003 is a rigid laminate; the bending study is a geometric simulation, and a physically bendable prototype would require a flexible substrate and re-tuning of the design.

B. Evidence Required and Present Status

Table XI. Evidence checklist for this work

Evidence	Status
S11 with marked band edges	Presented in Fig. 5
Explanation of incomplete UWB coverage	Qualitative hypotheses provided; parametric validation is not included
Patterns and gain at several frequencies	One radiation-pattern and gain set is presented; the corresponding frequency is unspecified
Mesh convergence study	Automatic mesh generation was used; convergence analysis is not documented
SAR at several frequencies and placements	Multi-frequency and multi-placement SAR evaluation is not presented
Flexible-substrate model or prototype	Flexible-substrate implementation and prototype validation are not presented
Measured S11, gain and patterns	Experimental measurement results are not included

Table XI lists the evidence that a complete wearable UWB study would contain and states honestly where this paper stands. Items marked missing are not supplied and are not replaced by estimates.

C. Planned AMC-Backed Stage

The shortfalls observed map directly to the next stage. An AMC placed behind the radiator is expected to increase gain and reduce SAR, as the EBG- and AMC-based studies indicate [5], [6], [7]. Closing the matching gaps will require tuning the slot dimensions, the bevel and the partial ground plane, since the deep 7.12 GHz resonance leaves room to trade depth for bandwidth. The low-current regions identified in Fig. 10 are natural candidates for reshaping. Further steps are a MIMO extension, machine-learning-assisted optimisation of slot and ground parameters, and fabrication and on-body measurement to validate the simulations. Table XII explains how the present results frame the targets of the AMC-backed stage. The benchmark values come from the reported EBG-backed design [5] and are indications of direction, not guaranteed outcomes.

Table XII. Present results and targets for the AMC-backed stage

Parameter	Present result	Direction for next stage
Peak gain	3.98 dB	Increase (benchmark 6.25 dBi [5])
SAR	1.2866 W/kg	Decrease (benchmark 0.695 W/kg [5])
UWB coverage	≈ 49 % of 7.5 GHz	Extend towards full 3.1–10.6 GHz
Footprint	60 × 60 mm	Keep compact; avoid thick backing
Bending	Retained at 30, 40 mm	Retain with backing in place
Validation	Simulation only	Fabricate and measure on body

(This work is licensed under a Creative Commons Attribution 4.0 International License.)

International Journal of Engineering Research & Technology (IJERT)
ISSN: 2278-0181
Vol. 15 Issue 10 , October - 2026

D. Expected Benefits and Risks of the Backing

Adding an AMC is not free of risk, and the next stage should be planned with both sides in view. The expected benefits are higher forward gain through in-phase reflection and lower SAR through suppression of backward radiation [5], [6]. The risks are fourfold. The AMC has its own useful band, typically narrower than the UWB range, so the combined antenna may be effective only where the AMC reflection phase is near zero. The nearby AMC changes the impedance seen by the radiator and can detune the matched bands that have been obtained here. The extra layer increases thickness and weight and reduces the bending tolerance that the planar radiator currently enjoys. And a periodic array is more sensitive to fabrication errors than a single printed layer, as noted for EBG-backed designs in the survey [5]. Each of these risks maps to a measurable item in the planned flow, namely the AMC reflection-phase band, the re-tuned S11, the bending repetition and the prototype measurement.

To guide the next iteration, Table XIII lists the main adjustable parameters and the effect each is expected to have, based on the role of each feature described in Section IV and on general UWB monopole practice. The entries are expectations to be tested by parametric sweeps, not results of this paper.

Table XIII. Tuning parameters and expected influence

Parameter	Expected influence
Bevel angle and length	Wideband transition; lower band edge; matching in gaps
Slot dimensions on patch	Position of extra resonances; depth of dips
Split ring and bell-slot size	Fine matching; resonances around 7 GHz
Partial ground length	Bandwidth versus backward radiation
Inset depth and gap	Input resistance at feed
AMC array and spacing	Gain increase; SAR decrease; added thickness

E. Planned AMC Design Flow

The next phase follows a conventional sequence. First, an AMC unit cell is designed on a grounded substrate and its reflection phase is simulated with periodic boundaries until the zero-phase crossing and the ±90° band cover the frequencies of interest. Second, the cells are assembled into an array whose size is a compromise between isolation and footprint. Third, the radiator of this paper is placed over the array at a small spacing and re-tuned, because the backing changes the impedance. Fourth, gain, pattern and SAR are re-evaluated with the same body model and placement so that the comparison with the present results is fair. Fifth, bending on 30 mm and 40 mm cylinders is repeated, since a layered structure is more sensitive to curvature than the planar radiator alone. Finally, a prototype is fabricated and measured in free space and on the body.

F. Threats to Validity

Several factors could change the reported numbers. Mesh density and solution settings influence simulated S11 and SAR, and conclusions should be confirmed by convergence checks. The SAR value depends on the tissue model, the separation between antenna and tissue and the input power, none of which is varied here. The bending study uses a rigid-substrate model on an idealised cylinder rather than a real wrist, so contact gaps, wrinkles and wrist motion are not represented. Finally, the comparison with literature relies on published results obtained under different conditions, so Table II indicates tendencies rather than a ranking.

G. Reproducibility

To support replication, the parameters that define the model are all given: the 60 × 60 × 1.6 mm RO4003 board, the 38 × 29.4 mm starting patch, the 10 mm × 3 mm × 1 mm inset feed, the 50 Ω lumped port, the airbox radiation boundary, the finite element solver and the 2–12 GHz sweep. The slot, split-ring and bell-slot dimensions are refined by simulation and will be tabulated in the fabrication-stage report, together with the mesh settings and the tissue model used for SAR.

VII. CONCLUSION

This paper presented the design and simulation-based evaluation of a compact, beveled Y-shaped monopole antenna intended for wearable off-body communication applications. The antenna was modelled on a Rogers RO4003 substrate with overall dimensions of 60 × 60 × 1.6 mm³ and incorporated slotted front- and rear-side metallisation, an inset feed, and a partial ground plane. Its electromagnetic characteristics were investigated using ANSYS HFSS 2025. The simulated reflection-coefficient response exhibited two resonant frequencies at 3.8 GHz and 7.12 GHz, with corresponding S11 values of −13.72 dB and −25.80 dB. The antenna achieved two impedance-matched frequency bands, extending from 3.43 to 4.51 GHz and from 5.79 to 8.39 GHz, based on the −10 dB criterion. These bands cover approximately 49% of the 3.1–10.6 GHz UWB allocation; therefore, the proposed structure should be considered a dual-band matched radiator within the UWB spectrum rather than a full-band UWB antenna. The simulated radiation characteristics showed an approximately omnidirectional pattern in the E-plane, with a reported peak gain of 3.98 dB and approximately 15 dB co-polarisation to cross-polarisation isolation. The surface-current distribution indicated current concentration around the bevel edges and feed region. The body-proximity evaluation produced a SAR value of 1.2866 W/kg for the simulated configuration, compared with the stated 1 g reference limit of 1.6 W/kg. This result should be interpreted only for the evaluated configuration because complete details of the tissue model, input power, and antenna-to-body separation are not available. Bending simulations using 30 mm and 40 mm cylindrical configurations were also considered; however, numerical resonance shifts are not available for quantitative comparison. The principal outcome of this work is the establishment of a simulated baseline for a compact beveled Y-shaped monopole and the documentation of its impedance, radiation, and available body-interaction characteristics. The present study is limited to numerical

(This work is licensed under a Creative Commons Attribution 4.0 International License.)

International Journal of Engineering Research & Technology (IJERT)
ISSN: 2278-0181
Vol. 15 Issue 10 , October - 2026

analysis, and no fabricated prototype or experimental measurements are reported. Furthermore, the rigid RO4003 substrate does not establish the physical flexibility required for a practical textile implementation. Future work will focus on developing and integrating an AMC backing structure to investigate its influence on forward radiation, gain, and SAR. The antenna geometry will also be further optimised to improve matching between the existing frequency bands and explore wider UWB coverage. Additional investigations should include a documented mesh-convergence study, complete SAR evaluation conditions, numerical bending comparisons, group-delay and pulse-fidelity analysis, and evaluation using a flexible substrate. Finally, prototype fabrication and measurements in free-space and representative on-body conditions will be necessary to verify the simulated results and establish the antenna's practical suitability for wearable off-body communication.

REFERENCES

[1] S. Douhi et al., "Metamaterial-integrated wearable UWB antenna with SAR reduction and gain enhancement for wireless body area sensor networks (WBASNs): Design and experimental verification," *Sensors and Actuators A: Physical*, vol. 388, Art. no. 116499, 2025, doi: 10.1016/j.sna.2025.116499.

[2] W. Thaiwirot et al., "The low-profile all-textile UWB antenna with AMC for WBAN applications," *Journal on Wireless Communications and Networking*, 2025, Art. no. 56, doi: 10.1186/s13638-025-02487-4.

[3] K. V. Karad et al., "A SAR analysis of hexagonal-shaped UWB antenna for healthcare applications," *Journal on Wireless Communications and Networking*, 2024, Art. no. 72, doi: 10.1186/s13638-024-02405-0.

[4] D. Sharma et al., "On-body and off-body communication using a compact wideband and high-gain wearable textile antenna," *Scientific Reports*, vol. 14, Art. no. 14493, 2024, doi: 10.1038/s41598-024-64932-6.

[5] Y. Thangavelu, B. Thangaraju, and R. Maheswar, "Design and SAR analysis of an AMC-integrated wearable cavity-backed SIW antenna," *Micromachines*, vol. 15, no. 12, Art. no. 1530, 2024, doi: 10.3390/mi15121530.

[6] P. A. Pathak et al., "A circular-shaped two-slot foam-based flexible UWB antenna for medical applications," *Journal on Wireless Communications and Networking*, 2024, Art. no. 89, doi: 10.1186/s13638-024-02420-1.

[7] M. Abdollahvand, "A novel and compact ultra-wideband printed monopole antenna with enhanced bandwidth and dual-band stop properties," *Microwave and Optical Technology Letters*, vol. 66, no. 1, Art. no. e33990, 2024, doi: 10.1002/mop.33990.

[8] G. K. Soni, D. Yadav, and A. Kumar, "A comprehensive review of wearable antenna design for on-body and off-body communication," *International Journal of Electronics and Telecommunications*, vol. 70, no. 2, pp. 525–532, 2024, doi: 10.24425/ijet.2024.149575.

[9] P. Chen, D. Wang, and Z. Gan, "Flexible and small textile antenna for UWB wireless body area network," *Micromachines*, vol. 14, no. 4, Art. no. 718, 2023, doi: 10.3390/mi14040718.

[10] A. A. R. Saad, W. M. Hassan, and A. A. Ibrahim, "A monopole antenna with cotton fabric material for wearable applications," *Scientific Reports*, vol. 13, Art. no. 7315, 2023, doi: 10.1038/s41598-023-34394-3.

[11] B. Kumkhet et al., "SAR reduction using dual-band EBG method based on MIMO wearable antenna for WBAN applications," *AEU—International Journal of Electronics and Communications*, vol. 160, Art. no. 154525, 2023, doi: 10.1016/j.aeue.2022.154525.

[12] M. T. Le, T. P. Tran, and Q. C. Nguyen, "Wearable BLE wireless sensor based on U-shaped EBG monopole antenna," *Journal of Sensors*, 2022, Art. no. 8593750, doi: 10.1155/2022/8593750.

[13] R. Li et al., "An EBG-based triple-band wearable antenna for WBAN applications," *Micromachines*, vol. 13, no. 11, Art. no. 1938, 2022, doi: 10.3390/mi13111938.

[14] D. Thangarasu et al., "On the design and performance analysis of flexible planar monopole ultra-wideband antennas for wearable wireless applications," *International Journal of Antennas and Propagation*, 2022, Art. no. 5049173, doi: 10.1155/2022/5049173.

[15] S. Jayakumar and G. Mohanbabu, "A wearable low-profile asymmetrical slotted ultra-wide band antenna for WBAN applications," *Journal on Wireless Communications and Networking*, 2022, Art. no. 103, doi: 10.1186/s13638-022-02186-4.

[16] "AMC integrated multilayer wearable antenna for multiband WBAN applications," *Computers, Materials & Continua*, vol. 71, no. 2, pp. 3227–3241, 2022, doi: 10.32604/cmc.2022.023008.

[17] P. R. Sura, M. Sekhar, and K. A. Kumar, "Design of dual-band notched UWB antenna loaded with split ring

(This work is licensed under a Creative Commons Attribution 4.0 International License.)

International Journal of Engineering Research & Technology (IJERT)
ISSN: 2278-0181
Vol. 15 Issue 10 , October - 2026

resonators for wide band rejection," *International Journal of Electronics Letters*, vol. 11, no. 1, pp. 17–29, 2023, doi: 10.1080/21681724.2021.2025437.

[18] O. P. Kumar, P. Kumar, and T. Ali, "A compact dual-band notched UWB antenna for wireless applications," *Micromachines*, vol. 13, no. 1, Art. no. 12, 2022, doi: 10.3390/mi13010012.

[19] M. M. Khan, A. Sultana, M. Masud, G. S. Gaba, and H. A. Alhumyani, "Miniaturized novel UWB band-notch textile antenna for body area networks," *Computer Systems Science and Engineering*, vol. 40, no. 3, pp. 1183–1198, 2022, doi: 10.32604/csse.2022.019872.

[20] "Design of compact monopole antenna with U-shaped defected ground structure (DGS) for UWB application," *Journal of Telecommunication, Electronic and Computer Engineering*, 2022, doi: 10.54554/jtec.2022.14.03.002.

[21] V. K. Rai and M. Kumar, "Tunable inverted U-shaped dual-band notch monopole antenna for ultrawideband applications," *IETE Journal of Research*, vol. 69, no. 7, pp. 4451–4460, 2023, doi: 10.1080/03772063.2021.1951373.

[22] "An ultrawideband antenna with two independently tunable notch bands," *Alexandria Engineering Journal*, vol. 79, pp. 402–410, 2023, doi: 10.1016/j.aej.2023.07.082.

[23] "Design and circuit analysis of a single and dual band-notched UWB antenna using vertical stubs embedded in feedline," *Heliyon*, 2021, doi: 10.1016/j.heliyon.2021.e08554.

[24] "Super compact UWB monopole antenna for small IoT devices," *Computers, Materials & Continua*, vol. 73, no. 2, pp. 2785–2799, 2022, doi: 10.32604/cmc.2022.028074.

[25] S. Rahim et al., "Super-UWB MIMO antenna with dual band-notched and high gain," *Radio Science*, 2022, doi: 10.1029/2022RS007501.

[26] G. V. Subrahmanyam and S. R. K. Kalva, "UWB monopole antenna with dual notched bands verified by characteristic mode analysis (CMA)," *Progress in Electromagnetics Research C*, vol. 121, pp. 39–48, 2022, doi: 10.2528/PIERC22051105.

[27] S. Mandal, S. K. Mandal, A. K. Mal, and R. Mahapatra, "A UWB dual band-notched on-chip antenna and its equivalent circuit model," *Progress in Electromagnetics Research B*, vol. 97, pp. 19–35, 2022, doi: 10.2528/PIERB22072602.

[28] "Dual band-notched ultra-wideband antenna with T-shape stub," *Electronics Letters*, vol. 58, no. 20, pp. 747–749, 2022, doi: 10.1049/ell2.12602.

[29] P. Pannu, "Highly compact UWB-MIMO antenna with sharp multi-stop band characteristics," *Journal on Wireless Communications and Networking*, 2024, Art. no. 48, doi: 10.1186/s13638-024-02369-1.

[30] "A compact UWB monopole antenna with triple band notches," *Micromachines*, vol. 14, no. 3, Art. no. 518, 2023, doi: 10.3390/mi14030518.

[31] Y. B. Chaouche, M. Nedil, I. B. Mabrouk, and O. M. Ramahi, "A wearable circularly polarized antenna backed by AMC reflector for WBAN communications," *IEEE Access*, vol. 10, pp. 12838–12852, 2022, doi: 10.1109/ACCESS.2022.3146386.

[32] "A PDMS-based low-profile monopole antenna for wearable applications," in *Proc. 2022 IEEE MTT-S International Microwave Biomedical Conference (IMBioC)*, 2022, doi: 10.1109/IMBioC52515.2022.9790236.

[33] "Design and realization of wearable textile slotted waveguide antennas," *Sensors*, vol. 23, no. 17, Art. no. 7509, 2023, doi: 10.3390/s23177509.

[34] "Fully textile dual-band logo antenna for IoT wearable devices," *Sensors*, vol. 22, no. 12, Art. no. 4516, 2022, doi: 10.3390/s22124516.

[35] "All-textile on-body antenna for military applications," *IEEE Antennas and Wireless Propagation Letters*, vol. 21, pp. 1065–1069, 2022, doi: 10.1109/LAWP.2022.3159301.

[36] P. B. Samal, S. J. Chen, and C. Fumeaux, "Wearable textile multiband antenna for WBAN applications," *IEEE Transactions on Antennas and Propagation*, vol. 71, pp. 1391–1402, 2023, doi: 10.1109/TAP.2022.3230550.

[37] "Breathable textile rectangular ring microstrip patch antenna at 2.45 GHz for wearable applications," *Sensors*, vol. 21, no. 5, Art. no. 1635, 2021, doi: 10.3390/s21051635.

[38] "Textile UHF-RFID antenna embroidered on surgical masks for future textile sensing applications," *IEEE Transactions on Antennas and Propagation*, vol. 70, pp. 5246–5253, 2022, doi: 10.1109/TAP.2022.3145477.

[39] H. Li, J. Du, X. X. Yang, and S. Gao, "Low-profile all-textile multiband microstrip circular patch antenna for WBAN applications," *IEEE Antennas and Wireless*

(This work is licensed under a Creative Commons Attribution 4.0 International License.)

International Journal of Engineering Research & Technology (IJERT)
ISSN: 2278-0181
Vol. 15 Issue 10 , October - 2026

Propagation Letters, vol. 21, pp. 779–783, 2022, doi: 10.1109/LAWP.2022.3146435.

[40] S. Vaezi, P. Rezaei, and A. A. Khazaei, "A miniaturized wideband wearable antenna with circular polarization for medical application," *AEU—International Journal of Electronics and Communications*, vol. 150, Art. no. 154197, 2022, doi: 10.1016/j.aeue.2022.154197.

[41] "A dual-band wearable conformal antenna based on artificial magnetic conductor," *International Journal of Antennas and Propagation*, 2022, doi: 10.1155/2022/9970477.

[42] J. Du, R. Wang, H. Li, and X. X. Yang, "All-textile compact ultra-wideband microstrip antenna with full ground plane for WBAN applications," *International Journal of Antennas and Propagation*, 2024, Art. no. 4236695, doi: 10.1155/2024/4236695.

[43] A. Praveena, G. Umamaheswari, J. K. Rai, and P. Ranjan, "Machine learning enabled compact flexible full ground UWB antenna for wearable applications," *International Journal of Microwave and Wireless Technologies*, 2024, doi: 10.1017/S1759078724000837.

[44] H. A. Muhammad, Y. I. Abdulkarim, P. A. Abdoul, and J. Dong, "Textile and metasurface integrated wide-band wearable antenna for wireless body area network applications," *AEU—International Journal of Electronics and Communications*, vol. 169, Art. no. 154759, 2023, doi: 10.1016/j.aeue.2023.154759.

[45] S. Varma, S. Sharma, M. John, R. Bharadwaj, A. Dhawan, and S. K. Koul, "Design and performance analysis of compact wearable textile antennas for IoT and body-centric communication applications," *International Journal of Antennas and Propagation*, 2021, Art. no. 7698765, doi: 10.1155/2021/7698765.

[46] A. De, B. Roy, A. Bhattacharya, and A. K. Bhattacharjee, "Bandwidth-enhanced ultra-wide band wearable textile antenna for various WBAN and Internet of Things (IoT) applications," *Radio Science*, vol. 56, no. 11, 2021, doi: 10.1029/2021RS007315.

[47] V. Marterer et al., "Wearable textile antennas: Investigation on material variants, fabrication methods, design and application," *Fashion and Textiles*, vol. 11, Art. no. 9, 2024, doi: 10.1186/s40691-023-00369-1.

[48] A. K. Biswas, S. Biswas, S. Haldar, and A. Nandi, "A highly decoupled flexible 4-element MIMO antenna with band-notched characteristics for ultra-wide-band wearable applications," *AEU—International Journal of Electronics and Communications*, vol. 173, Art. no. 154985, 2024, doi: 10.1016/j.aeue.2023.154985.

[49] P. Bhardwaj and R. K. Badhai, "Annular ring UWB wearable textile antenna for telemetry and healthcare applications," *IETE Journal of Research*, vol. 70, no. 6, pp. 5525–5539, 2024, doi: 10.1080/03772063.2023.2258512.

[50] A. Maria and P. Mythili, "Compact UWB wearable textile antenna for on-body WBAN applications," *Progress in Electromagnetics Research B*, vol. 105, pp. 43–57, 2024.

(This work is licensed under a Creative Commons Attribution 4.0 International License.)